ACS Catalysis

Research Article

Cite This: ACS Catal. 2019, 9, 9499−9507

pubs.acs.org/acscatalysis

Highly Effective Propane Dehydrogenation Using Ga−Rh Supported Catalytically Active Liquid Metal Solutions

Narayanan Raman,[†,¶] Sven Maisel,[‡,¶] Mathias Grabau,[§] Nicola Taccardi,[†] Jonas Debuschewitz,[†] Moritz Wolf,[†] Haiko Wittkämper,[§] Tanja Bauer,[∥] Mingjian Wu,[⊥] Marco Haumann,[†] Christian Papp,[§] Andreas Görling,[‡] Erdmann Spiecker,[⊥] Jörg Libuda,[∥] Hans-Peter Steinrück,[§] and Peter Wasserscheid*[,†,#]

[†]Lehrstuhl für Chemische Reaktionstechnik (CRT), [‡]Lehrstuhl für Theoretische Chemie, [§]Lehrstuhl für Physikalische Chemie II, and [∥]Lehrstuhl für Katalytische Grenzflächenforschung, Friedrich-Alexander-Universität Erlangen-Nürnberg (FAU), Egerlandstr. 3, 91058 Erlangen, Germany

[⊥]Lehrstuhl für Werkstoffwissenschaften, Mikro- und Nanostrukturforschung, Friedrich-Alexander-Universität Erlangen-Nürnberg (FAU), Cauerstr. 6, 91058 Erlangen, Germany

[#]Forschungszentrum Jülich, "Helmholtz-Institute Erlangen-Nürnberg for Renewable Energies" (IEK 11), Egerlandstr. 3, 91058 Erlangen, Germany

Supporting Information

ABSTRACT: Our contribution demonstrates that rhodium, an element that has barely been reported as an active metal for selective dehydrogenation of alkanes becomes a very active, selective, and robust dehydrogenation catalyst when exposed to propane in the form of single atoms at the interface of a solid-supported, highly dynamic liquid Ga−Rh mixture. We demonstrate that the transition to a fully liquid supported alloy droplet at Ga/Rh ratios above 80, results in a drastic increase in catalyst activity with high propylene selectivity. The combining results from catalytic studies, X-ray photoelectron spectroscopy, IR-spectroscopy under reaction conditions, microscopy, and density-functional theory calculations, we obtained a comprehensive microscopy picture of the working principle of the Ga−Rh supported catalytically active liquid metal solution.

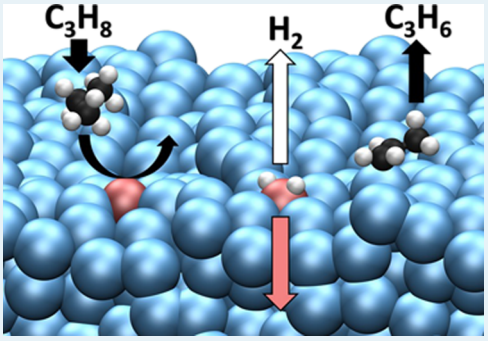

KEYWORDS: *catalysis, dehydrogenation, alkane, alkene, gallium, rhodium*

INTRODUCTION

Following our general interest in novel supported liquid catalysts for high temperature applications, we have very recently proposed supported catalytically active liquid metal solutions (SCALMS) as a very promising class of heterogeneous catalysts. Published SCALMS systems are composed of catalytically active liquid alloy droplets (Ga_xPd_y[1,2] or Ga_xPt_y[3]) on a porous support. In contrast to conventional supported liquid phase catalysis, the catalytic reaction in SCALMS occurs only at the highly dynamic liquid metal/gas interface, as the liquid metal does not provide any relevant reactant solubility. The first account of SCALMS systems in catalysis[1] described Ga-rich Ga/Pd mixtures (Ga/Pd ratio > 10) on porous glass and revealed high activity and high robustness of these systems against coking in *n*-butane dehydrogenation at 450 °C. The liquid nature of the supported alloy droplet under the reaction conditions was confirmed through a combination of X-ray diffraction, scanning electron microscopy (SEM), X-ray photoelectron spectroscopy (XPS), and ab initio dynamics calculations.

Shortly after our initial SCALMS work was published, Upham et al. reported a bulk liquid metallic solution of nickel in bismuth, which could be used up to temperatures of 1100 °C for methane pyrolysis to hydrogen and elemental carbon.[4] These authors showed that the activity and stability of the bulk liquid metallic catalyst were higher than that of its solid counterparts. While a Ni wire lost 50% of its activity in less than 1 h, the bulk liquid metallic catalyst could be used up to 1200 h, without any significant loss of performance. With their findings, these authors confirmed general statements in earlier works by Ogino, claiming that the intrinsic dynamics of liquid metal surfaces would help to avoid the loss of activity in bulk liquid metal catalysis.[5] Severe corrosion issues, however, arise when operating bulk liquid metals and their alloys in contact with metallic reaction equipment, making this sort of bulk liquid metal catalysis challenging from an application point of view.[6]

So far, only a small number of examples of rhodium-based alkane dehydrogenation catalysts have been reported. The excellent and very comprehensive review on alkane dehydro-

Received: June 12, 2019
Revised: August 26, 2019
Published: September 6, 2019

DOI: 10.1021/acscatal.9b02459
ACS Catal. 2019, 9, 9499−9507

genation published by Sattler et al. from 2014[7] does not contain a single example of Rh-based alkane dehydrogenation catalysis. Our own targeted literature survey revealed only two papers dealing with the dehydrogenation of iso-butane using Rh-based catalysts.[8,9] In both papers, the activity of the Rh systems was reported to be much lower compared to Pt- or Pd-based catalysts on the same supports.[10]

In this contribution, we present a new Ga−Rh SCALMS system exhibiting highly attractive catalytic performance in propane dehydrogenation (PDH). To the best of our knowledge, no example of Rh-catalyzed dehydrogenation of propane has been reported. Our contribution focuses on three different states of the investigated Rh-based catalysts and aims to pinpoint characteristic differences among them: (i) single phase Rh on alumina as a baseline comparison of a traditional supported Rh catalyst. (ii) Alumina-supported Ga−Rh with an atomic Ga/Rh ratio of 25 and 34. According to the Ga−Rh phase diagram,[11] these compositions lead to the formation of a mixture of solid intermetallic Ga−Rh compounds (e.g., $Ga_{16}Rh_3$) and a liquid Rh−Ga-rich alloy at the highest reaction temperatures tested (550 °C). (iii) Alumina-supported Ga−Rh with an atomic Ga/Rh ratio above 80. These highly diluted compositions result in supported, fully liquid droplets of the Ga−Rh alloy at a temperature of 550 °C.[11]

We demonstrate that the addition of Ga to the alumina-supported Rh catalyst leads to an enhanced catalytic performance. Interestingly, a strong additional boost in Rh-based activity can be found at the transition to the fully liquid Rh−Ga system. We performed XPS, IR-spectroscopy, and microscopy studies in combination with density-functional calculations to reveal how catalysis at the liquid interface of Rh−Ga SCALMS systems proceeds at the microscopic level.

RESULTS AND DISCUSSION

Synthesis of Ga−Rh-SCALMS Materials. The Ga−Rh SCALMS materials were prepared using the procedure recently described for Ga/Pd systems.[1] Analogously, the deposition of Rh was achieved by partial galvanic replacement of Ga. Briefly, aqueous suspensions of the metallic Ga/AlO_x material were mixed with different amounts of stock solution of $RhCl_3 \cdot 3H_2O$, in order to obtain the materials with the intended different Rh−Ga ratios. After filtration, the products were dried at 130 °C and used in the catalytic experiment without any further treatment (for details see Supporting Information).

PDH Experiments. The PDH experiments were carried out in a tubular quartz reactor. The reactor was heated to the desired reaction temperature under a flow of an inert gas. When the reaction temperature was reached, a flow of propane was added to the He flow, resulting in a catalyst bed contact time of 0.7 s and a gas hour space velocity (GHSV) of 4900 h^{-1}. The effluent gas flow was analyzed with an online-GC (see Supporting Information for details).

Figure 1 shows the comparison of Rh on alumina with the Ga−Rh alloys of different compositions (as prepared in this work) at 550 °C. Rh on alumina displays under these conditions an initial productivity of 15 $g_{propylene}\ g_{Rh}^{-1}\ h^{-1}$ that remains stable over 15 h time-on-stream. The conversion with the Rh/AlO_x catalyst is around 4% with propylene selectivity rising from an initial 78% level to close to 90% after 15 h time-on-stream. Note, that the empty reactor shows a conversion of around 0.3% with a propylene selectivity of 35% at 550 °C

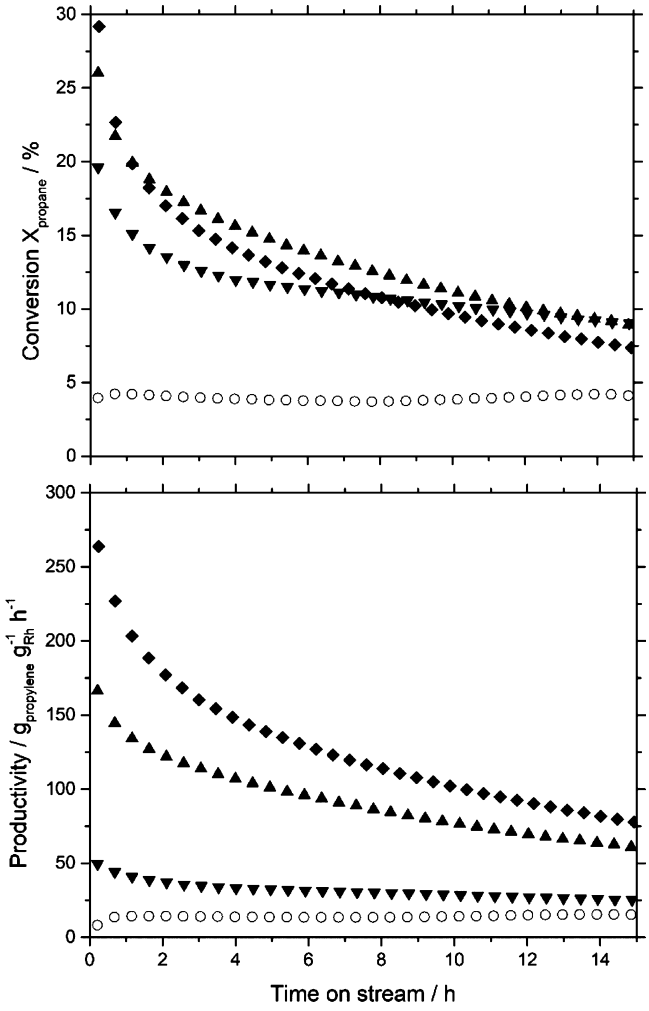

Figure 1. Conversion (top) and Rh-based productivity (bottom) of different Ga−Rh-SCALMS in PDH at 550 °C and 1.2 bar. Molar ratios of Ga−Rh are 0 (open circles), 34 (downward-pointing triangles), 89 (upward-pointing triangles), and 125 (diamonds). Reaction conditions: 1.2 g catalyst (Rh/Al_2O_3: 0.19 wt % Rh; $Ga_{34}Rh$: 0.26% Rh, 5.90% Ga; $Ga_{82}Rh$: 0.11% Rh, 5.9% Ga; $Ga_{125}Rh$: 0.07% Rh, 5.94% Ga), He flow 89 $mL_N\ min^{-1}$, C_3H_8 flow 8.9 $mL_N\ min^{-1}$, GHSV 4900 h^{-1}.

(propane flow: 8.9 mL min^{-1}, He flow: 89 mL min^{-1}, see Supporting Information for further details).

As the baseline experiment, we also evaluated the catalytic activity of Ga on AlO_x at 550 °C in PDH. It was found that the initial conversion was 4% with a propylene selectivity of around 95%. Note, that gallium oxide has recently been described as an active catalyst for PDH.[12,13] We cannot exclude that some amount of gallium oxide is present in the precious metal-free, Ga on the AlO_x material in the form of a passivation layer of the Ga droplets adsorbed on the support, and that this amount caused the observed catalytic activity. However, it is known from the literature that in the presence of noble metals under the reductive conditions of PDH experiments, gallium oxide species are reduced to elemental Ga.[14,15] Indeed, we find clear evidence from our XPS and IR spectroscopy experiments that gallium oxide species are reduced to elemental Ga in the presence of Rh (see below and Supporting Information). All Ga−Rh alloys under investigation showed significantly higher initial conversions, with ∼20% ($Ga_{34}Rh$), and ∼29% ($Ga_{125}Rh$).

DOI: 10.1021/acscatal.9b02459
ACS Catal. 2019, 9, 9499−9507

Comparing the catalytic performance of the Ga−Rh alloys with maximum and minimum compositions ratios (125 vs 34) at 550 °C, a remarkable difference in productivity is observed. This change in alloy composition resulted in a productivity increase by a factor of 4−5. The maximum initial activities were 263 $g_{propylene}\ g_{Rh}^{-1}\ h^{-1}$ versus 49 $g_{propylene}\ g_{Rh}^{-1}\ h^{-1}$, for $Ga_{125}Rh$ and $Ga_{34}Rh$, respectively, and the productivities after 15 h time-on-stream were 127 $g_{propylene}\ g_{Rh}^{-1}\ h^{-1}$ versus 31 $g_{propylene}\ g_{Rh}^{-1}\ h^{-1}$, respectively. Selectivities were very similar in all experiments with Ga−Rh alloys: typically around 92% for conversions between 10 and 20% (see Supporting Information for details). All SCALMS material showed slight deactivation over time. No apparent changes in the catalyst morphology could be seen by means of SEM imaging, for example droplet coalescence with consequent loss of the active surface (see Supporting Information, Figure S3). However, deactivation due to morphological changes cannot be completely excluded. On the other hand, the observed deactivation could be attributed to the formation of coke under reaction conditions, that is, at 550 °C. Indeed, XPS of spent catalysts showed an increase of the C 1s component in all samples when compared to the as-prepared materials (see Supporting Information, Figure S11). In addition, the presence of coke in SCALMS after PDH was confirmed using Raman spectroscopy (see Supporting Information, Figure S10). However, the moderate fluorescence of Al_2O_3 due to the applied laser wavelength prohibited the clear identification of coke in spent SCALMS after PDH at a temperature ≤ 500 °C, suggesting a minor formation of carbon on these catalysts under these milder conditions. Remarkably and in strong contrast to the tested SCALMS, the formation of coke was clearly observable for the Ga-free Rh catalyst after PDH, already at the lowest temperature tested of 450 °C (i.e., indicating the deposition of a sufficient amount of coke to quench the fluorescence of Al_2O_3). In other words, although the formation of coke could not be completely suppressed, the SCALMS materials displayed an increased resistance against coking compared to the pure Rh catalyst used as the benchmark. In fact, the formation of a detectable amount of carbon on SCALMS could be only observed under the most severe conditions applied, that is, running the PDH at 550 °C. Accordingly, we suggest that the observed conversion with the Ga-free Rh catalyst is just the residual activity after substantial coking deactivation. While the SCALMS systems, conversely, show strongly enhanced performance over a long time on stream operations, as the poisoning by coke formation is significantly reduced (Figure 1).

XPS Investigations. The XPS measurements of the supported alloy samples, before and after catalytic operation, clearly indicate the formation of metallic Ga and Rh species [Ga, Rh, or intermetallic compounds (IMCs)] during the reaction (see Supporting Information for details). Moreover, to understand the surface behavior/composition of Rh−Ga alloy droplets, we also studied model alloy samples with compositions comparable to those screened in the catalytic tests, as a function of temperature under ultrahigh vacuum conditions.

In Figure 2, the temperature-dependent composition, as obtained from the quantitative analysis of the XP spectra, is shown for the three different mixtures $Ga_{166}Rh$, $Ga_{82}Rh$, and $Ga_{49}Rh$ (0.6, 1.2, and 2.0 at. % Rh in Ga); for exemplary XP spectra collected from a sample of composition $Ga_{82}Rh$ see the Supporting Information, Figure S13.

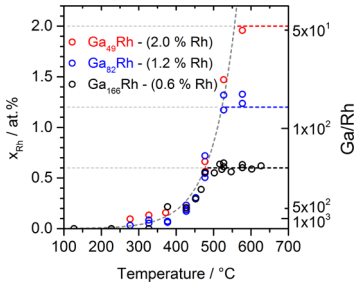

Figure 2. Rh atomic fraction from quantitative XPS as a function of the sample temperature. Three curves are shown for the $Ga_{166}Rh$, $Ga_{82}Rh$, and $Ga_{49}Rh$ samples (0.6, 1.2, and 2.0 at. % Rh in Ga).

The measured composition is representative for the composition of the liquid phase because of the rather high information depth in lab-based XPS (93 Å for Ga 3d, 77 Å for Rh 3d in Ga). The temperature-dependent change of Rh intensity is ascribed to the formation or melting of Rh-rich IMC, which form in the bulk of the Ga−Rh droplet or at the droplet interface with alumina (see also microscopy results below) at lower temperatures. These solid IMC phases, present in the bulk of the liquid have macroscopic dimensions and are not probed by the surface-sensitive XPS measurement of the droplet. A similar behavior and analysis was recently reported for the Ga−Pd system at low Pd concentrations.[1,16] For compositions of $Ga_{166}Rh$ and $Ga_{82}Rh$ (0.6 and 1.2 at. % Rh in Ga), the respective plateaus at 480 and 530 °C indicate that the liquidus temperature (where all IMC are dissolved, and the XPS data thus give the nominal bulk concentration) is reached, see Figure 2. Below the liquidus temperature, the composition of the liquid phase is given by the concentration on the liquidus line. Here, we observe a qualitative agreement with the bulk phase diagram of Rh−Ga, and the bulk phase diagrams of comparable systems (Pt−Ga, Pd−Ga). For $Ga_{49}Rh$, the measurement at the highest temperature also reached the nominal bulk composition.

Microscopic Investigations. To further elucidate the structure, composition, and phase stability of the Ga−Rh systems under investigation, microscopy investigations on Ga−Rh model nanoalloys were carried out with transmission electron microscopy (TEM), either static at room temperature (RT) or in situ during heating using a furnace TEM holder. Together with the XPS analysis, these investigations are particularly valuable as the phase diagram of the Ga−Rh system is not safely established in the low Rh concentration range.[11,17] Moreover, phase stability and melting points may be altered for bimetallic nanoparticles by nanoscale effects.[18] TEM studies were performed on a series of model Ga_xRh_1 nanoalloys (with x = 16−160, i.e., Rh 0.6−6 at. %) supported on thin SiO_2 membranes. Details on the preparation of the alloy nanoparticles by physical vapor deposition are provided in the Supporting Information.

We first describe the structural properties at RT. A typical two-phase structure of crystalline (c-) precipitates in amorphous (a-) nanoparticles is found throughout all samples, and exemplary results from the sample with x = 36 (Rh = 2.7 at. %) are summarized in Figure 3a−c. By combining EDXS mapping, quantification, and careful analysis of the sharp diffraction rings in electron diffraction patterns, the crystal phase is identified as $Ga_{16}Rh_3$ or $Ga_{21}Rh_4$ and their derivatives (see Supporting Information for details). The crystallites possess a laminate shape and show a preferential orientation,

DOI: 10.1021/acscatal.9b02459
ACS Catal. 2019, 9, 9499−9507

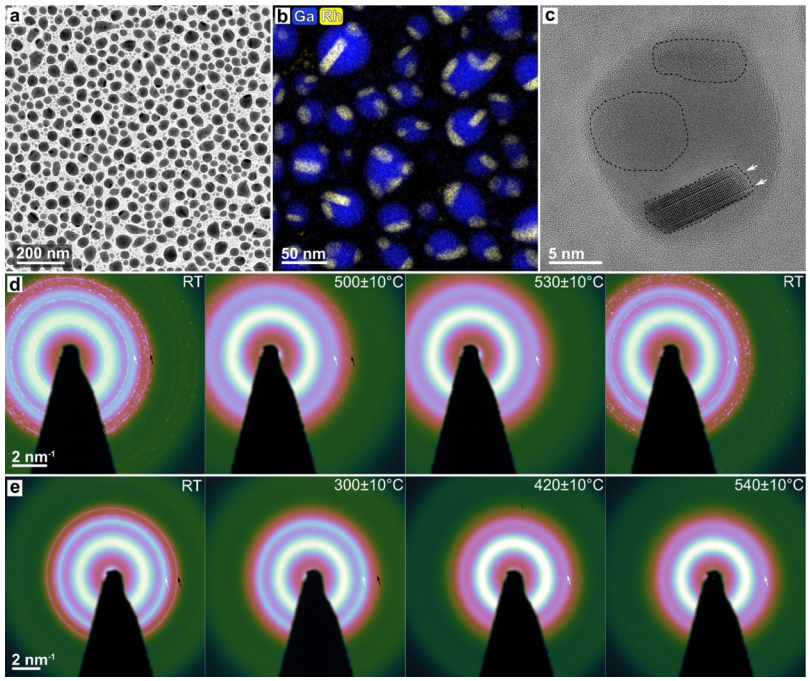

Figure 3. Static (a–c) and in situ (d,e) TEM investigations of the structure, chemical composition, and temperature-dependent phase properties of Ga–Rh nanoparticles. (a) BF-TEM image of the particles prepared on the thin SiO_2 membrane. The particles contain crystalline precipitates as revealed by dark diffraction contrast. (b) Composed Ga and Rh map extracted from a scanning TEM–EDX dataset confirming an increased Rh concentration (~12–15 at. %) in the areas showing precipitates. (c) HRTEM image of a single Ga–Rh particle, the dashed circles indicate the crystalline Ga–Rh phase. Key frames of electron diffraction patterns taken during an in situ heating experiment from the samples with (d) x = 36 (Rh = 2.7 at. %) and (e) x = 36 (Rh = 2.7 at. %). Temperatures are indicated at the top-right corner of each pattern. See the text for details, complete time series (movie) of in situ SAED are provided in Supporting Information.

which is likely due to the presence of the SiO_2 membrane below. Stacking disorder can often be seen in the laminates (cf. Figure 3c white arrows). The Ga-rich particle matrix shows an amorphous contrast in the high-resolution TEM (HRTEM) image, which agrees with the broad diffuse rings in the electron diffraction patterns (see Supporting Information, Figure S15). With increasing Rh concentration from 0 to 6 at. % a systematic evolution of the particle size and shape toward a larger size with a more irregular shape is found (see Supporting Information, Figure S16).

From the sparse literature on Ga–Rh systems, the (equilibrium) melting temperature at the low Rh concentrations studied in the present work is expected to be in the range of 200–600 °C.[11] To elaborate the phase stability of the c-Ga_xRh_y/a-Ga–Rh nanoparticles, electron diffraction has been performed in situ while heating the samples in the TEM. Figure 3d,e show key frames from a series of in situ electron diffraction patterns taken from the samples with x = 36 (Rh = 2.7 at. %) and x = 105 (Rh = 0.9 at. %), respectively. In the sample with x = 36, many sharp diffraction rings (exemplarily marked by black arrows in the respective patterns) from nanoscale c-Ga_xRh_y can be clearly seen from RT (Figure 3d, left) up to 480 ± 10 °C. These sharp rings fade out at a temperature of 500 ± 10 °C and are completely absent at 530 ± 10 °C (Figure 3d, center). Upon slow cooling down to RT (over a period of about 3 min), the sharp crystalline ring gradually reappeared resulting in a pattern at RT which matches well to that before heating. After cooling down to RT, the microstructure and Ga to Rh ratio returned to almost the same value as before heating (Figure 3d, rightmost and Supporting Information), indicating negligible sublimation of Ga and/or Rh in the vacuum environment of the TEM. In the sample with x = 105, the sharp crystal rings are much less pronounced as expected from the lower amount of the crystalline phase. In a few cycles of heating/cooling experiments, the crystal rings disappeared/appeared at temperatures between 300 and 420 °C. We state here that the disappearing/appearing of sharp diffraction rings is not necessarily associated with a solid–liquid phase transformation. A detailed analysis of two broad diffraction rings that can in addition be seen at positions q = 2.6 and 4.2 nm^{-1} is given in Supporting Information.

Density-Functional Calculations Elucidating the Mode of Action of the Ga–Rh SCALMS Systems in PDH. To gain further insight into the nature of the catalytic phase, its surface composition and the active site for the catalytic transformation, we carried out ab initio molecular dynamics (AIMD) simulations based on density-functional theory (DFT) with periodic boundary conditions. An estimation of the uncertainty of the AIMD simulations can be found in Supporting Information.

In detail, we studied the composition of the surface using a slab model with a tetragonal simulation box containing 180 atoms with a Ga–Rh ratio of 89 (178 Ga, 2 Rh atoms) and Rh initially located at the surface (one Rh at each side of the slab). The time evolution of the z-position of Rh atoms in the slab is shown in Figure 4a (green curve). It is obvious that already after a few picoseconds Rh disappears from the surface. This is in line with a simulation with the Ga–Rh ratio of nine (162 Ga, 18 Rh atoms) that shows a Rh surface depletion (see Supporting Information, Figure S21). However, in order to be catalytically active, the rare Rh surface atoms have to stay at the surface if a reactant or reaction intermediate is adsorbed on them. To probe this, we ran AIMD simulations starting with

DOI: 10.1021/acscatal.9b02459
ACS Catal. 2019, 9, 9499–9507

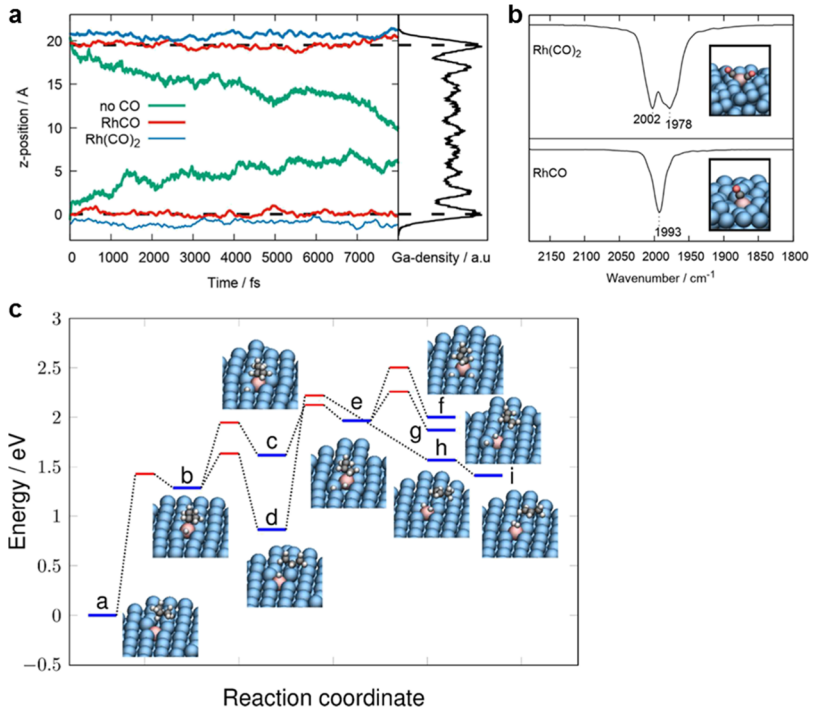

Figure 4. Results from DFT calculations. (a) *z*-position (perpendicular to the surface) of Rh atoms in the liquid slab model (see main text and Supporting Information) as function of time. The Rh atoms were initially located at the two surfaces of the slab, one at the top and one at the bottom surface. The green lines correspond to a simulation without any adsorbate attached to the Rh atoms at the surface. The red and the blue lines correspond to a starting configuration for the simulations, where one and two CO molecules are adsorbed at each of the Rh atoms at the surface. On the right the Ga-density along the *z*-direction of the slab is shown for orientation. Horizontal lines indicate the first maximum of the Ga-density for the two surfaces. (b) Simulated vibrational power spectra for $Rh(CO)_2$ (upper part) and RhCO (lower part); snapshots of one corresponding geometry from the MD simulations are additionally depicted. (c) Reaction diagram for the dehydrogenation of propane on fcc-Ga(100) with one Rh ad-atom. Ga is depicted in blue, Rh in light red, C in black, and H in white. Reaction intermediates are indicated by blue lines and transition states by red lines.

Rh plus an attached adsorbate located at the surface. For all tested adsorbates, namely, one or two CO molecules (Figure 4), a propyl residue with one additional hydrogen atom, propylene, and a hydrogen molecule (see Supporting Information, Figure S22) the adsorbed species can retain Rh at the surface until it desorbs. After desorption of the adsorbed species, the Rh atoms immediately diffuse away from the surface. As will be shown later, DFT calculations suggest that at the end of the dehydrogenation, propylene is adsorbed to Ga atoms, whereas H_2 is bound to the catalytically active Rh atom. Once H_2 is desorbed, Rh immediately moves from the surface into the Ga matrix. The fact that adsorbates can hold dynamically appearing Rh atoms at the surface may lead to a certain enrichment of catalytically active centers during catalysis.

To further elucidate the mechanism of PDH with our Ga−Rh SCALMS catalyst, we constructed a solid model system consisting of a face-centered cubic (fcc)-Ga(100) surface with one Rh atom located in a slightly distorted fourfold surface hollow site to represent the isolated catalytically active center. We choose this system for two reasons: (1) the partial radial distribution function between Rh and Ga was calculated from the MD simulation for the slab model used in the MD simulations as described before. Here, the maximum of the peak corresponding to the first coordination sphere of Rh is located at a distance of 2.54 Å away from Rh. In comparison with this, the Rh adatom in the distorted hollow-site of the fcc-Ga(100) is on average 2.50 Å away from its neighboring Ga atoms. (2) In addition, we calculated Bader charges for the liquid system used in the MD as well as the solid model system with the result that Rh in both cases is negatively charged (−0.83 e as average in the MD simulation, −0.82 e in the solid model). DFT geometry optimizations were performed in combination with the climbing image-nudged elastic band (cNEB) approach and the dimer method[19,20] to determine reaction barriers between possible reaction intermediates (see Supporting Information for details). Additionally, we carried out calculations for free energies and barriers. The corresponding reaction profile is shown in the Supporting Information and agrees very well with the energies and barriers without free energy corrections. The corresponding reaction diagram for some potential pathways is shown in Figure 4c. Note that this is the first step to get insight into the basic reaction mechanism of the dehydrogenation at the atomic level using a specific slab model in conjunction with the cNEB technique to determine the transition-state energies. Further details of the reaction mechanism could be obtained in future work for example by advanced, computationally very demanding MD methods. In the initial step, the first C−H bond of the weakly bound propane (Figure 4c (a), $E_{ads} \approx 0.46$ eV) breaks with an activation barrier of 1.42 eV leaving both H and the residual 2-propyl species bound to the surface Rh atom (b). The subsequent diffusion of hydrogen to an adjacent Ga atom (c) is calculated to have a larger energy barrier (0.66 eV) than the diffusion of the 2-propyl residue (d, 0.32 eV) because of the large affinity of hydrogen to Rh. The resulting geometry (d) is 0.76 eV more stable than the structure (c). To complete the dehydrogenation starting from (d), a rotation of 2-propyl is

DOI: 10.1021/acscatal.9b02459
ACS Catal. 2019, 9, 9499−9507

Table 1. Experimentally Observed and DFT-Derived Peaks and Assignments for All Examined Ga_x-Rh_y/Al_2O_3 Samples (for Details See Supporting Information)

sample	peak position/cm^{-1}	assignment	based on refs
		DRIFT Spectra	
Rh/Al_2O_3	2093	$Rh^I(CO)_2-\nu_{as}(CO)$ (asym. stretching mode)	26,29,31
	2023	$Rh^I(CO)_2-\nu_s(CO)$ (sym. stretching mode)	26,29,31
	2065	Rh^0CO	26,28
$Ga_{25}Rh_1/Al_2O_3$ (see Supporting Information)	2099, 2021	$Rh^I(CO)_2-\nu_{as}(CO)$, $\nu_s(CO)$	26,29,31
	2100, 2088, 2072, 2054, 2031	RhCO (in a Ga environment/on IMC)	
$Ga_{88}Rh_1/Al_2O_3$	2092, 2018	$Rh^I(CO)_2-\nu_{as}(CO)$, $\nu_s(CO)$	26,29,31
	2056	Rh^0CO	26,28
	2024	$Ga-H/Rh(CO)_2$ ($\nu_{as}(CO)$ in liquid Ga, DFT)	DFT
	1974	RhCO (small deposits on Al_2O_3)	32
	1993	RhCO (in liquid Ga, DFT)/$Rh(CO)_2$ ($\nu_s(CO)$ in liquid Ga, DFT)	DFT
$Ga_{125}Rh_1/Al_2O_3$ (see Supporting Information)	2095, 2024	$Rh^I(CO)_2-\nu_{as}(CO)$, $\nu_s(CO)$	26,29,31
	2057	Rh^0CO	26,28
	2027	Ga−H	25
Ga/Al_2O_3	2021	Ga−H	25
	∼1880	$Ga^{\delta+}-H$	25
		DFT Frequencies	
Rh(111)	2067, 2025, 2002, and 1994	ν(CO) at top-sites 3/4, 1/4, 1/9 and 1/16 of a CO monolayer	
Rh−CO (in Ga slab)	1993		
$Rh-(CO)_2$ (in Ga slab)	2002, 1978	$Rh^I(CO)_2-\nu_{as}(CO)$, $\nu_s(CO)$ (in Ga)	

required such that a hydrogen of the terminal carbon atom is in proximity to Rh, with subsequent C−H bond breaking. The activation barrier for this process is calculated to be 1.31 eV, leading to geometry (h). In addition, we investigated the second C−H bond breaking starting from the less stable structure (c), which follows a similar pathway to the first C−H dissociation; first, the C−H bond breaks with an activation barrier of 0.54 eV with both, hydrogen and propylene bound to Rh (e). Thereafter, the diffusion of propylene to the adjacent Ga (g) requires a lower activation energy (0.29 eV) than hydrogen diffusion (f) (0.52 eV). Considering the final geometries, it is obvious that the more hydrogen is bound to Rh, the more energetically favorable is the structure. This suggests (i) that at the end of the dehydrogenation reaction, propylene is bound to Ga atoms and can diffuse away from the active Rh and desorb in the gas phase, while the resulting two H atoms bound to Rh recombine and desorb as H_2. From our mechanistic study, we conclude that the reaction proceeds as follows: in the first step, propane that comes from the gas phase with high kinetic energy hits the reactive Rh center at the surface and uses its kinetic energy for the first dehydrogenation step. The other reaction steps require smaller barriers, which can easily be overcome at elevated temperatures. At the end of the reaction, propene diffuses onto the Ga matrix and can desorb. Hydrogen at the Rh center can recombine and desorb as H_2. After the H_2 desorption, our AIMD simulations show that the Rh atom immediately moves away into the Ga matrix. To further investigate the origin of the catalytic activity of SCALMS, we calculated Bader charges for the liquid SCALMS model as well as the Rh(111) surface to compare the Rh species in the Ga environment with metallic Rh of the Rh(111) surface. We found that the Rh in the liquid Ga slab has an average charge of −0.83 e in the MD simulation, while in the Rh(111), the surface Rh atoms are obviously metallic Rh^0 species. We conclude that Ga plays the role of an electron donor for the more electronegative Rh. The negatively charged Rh species, in contrast to Rh^0, is a strongly active dehydrogenation catalyst. This also is one explanation why the Rh/AlO_x catalyst shows a significantly lower conversion than SCALMS catalysts. Furthermore, this emphasizes the important role of the Ga matrix for the catalytic process.

Besides this, Ga also modifies the adsorption properties of the reactants. One of the main issues in dehydrogenation catalysis, for example for industrially used Pt/AlO_x catalysts, is coking of the surface because the desired products like propene bind to the active sites too strongly and therefore desorption is hindered and further dehydrogenation or cracking reactions can occur, which lead to undesired side products and coking of the surface. This can be prevented by lowering the adsorption strength of the desired products, which in this case is achieved by the Ga matrix around the catalytically active center. Our calculated mechanism also shows that it is thermodynamically more stable for propene to diffuse away from the reactive Rh center to the Ga matrix, while hydrogen stays at Rh. Propene can then easily diffuse away from the Ga matrix. Again, this underlines the importance of the Ga matrix in the SCALMS system.

Infrared Spectroscopy. Finally, we performed in situ infrared spectroscopy to gain further information on the state of Rh in the catalytically active SCALMS. We probed the noble metal sites at the Ga−Rh interface with adsorbed CO and investigated Ga−Rh alloys of various compositions ($Ga_{25}Rh$, $Ga_{88}Rh$, and $Ga_{125}Rh$ on Al_2O_3), monometallic Ga/Al_2O_3, and Rh/Al_2O_3 as a reference. Both experiments and DFT calculations showed that elemental Ga is inactive toward CO adsorption,[21−24] while experimental data showed the presence of hydrides.[25] Rh, in contrast, shows rich carbonyl chemistry, especially when supported on oxides. The two main features observed on such systems are CO bound to metallic Rh in an on-top fashion (Rh^0CO)[26−28] and the atomically dispersed dicarbonyl $Rh^I(CO)_2$ formed via the oxidative disruption of metallic Rh particles.[26,29−32] Most bands on the Rh and Rh−

DOI: 10.1021/acscatal.9b02459
ACS Catal. 2019, 9, 9499−9507

Ga samples can be assigned based on previous studies (see assignments summarized in Table 1).

Here, we limit the discussion to samples with low Rh loading. Figure 5 shows the DRIFT spectra obtained from

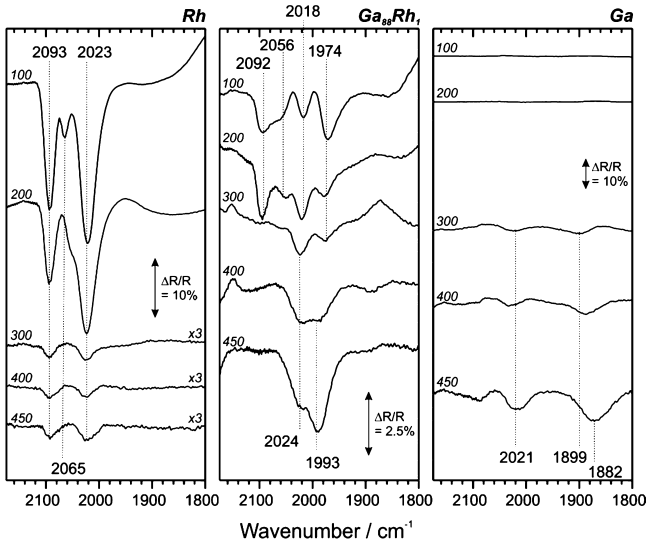

Figure 5. CO-stretching region of the DRIFT spectra obtained from $G_{88}Rh/Al_2O_3$ and monometallic Ga−Rh samples in an Ar atmosphere after treatment with CO. The temperature in °C and the scaling factors are indicated on the left and right side of each panel, respectively. All spectra were normalized and displayed as difference spectra as described in the Supporting Information.

$Ga_{88}Rh_1/Al_2O_3$ and monometallic Ga−Rh samples. The spectra acquired from $Ga_{25}Rh_1/Al_2O_3$ and $Ga_{125}Rh_1/Al_2O_3$ are provided in the Supporting Information (Figure S26) together with a detailed discussion of all DRIFT experiments.

For the Ga_{88}−Rh_1/Al_2O_3 sample, the bands at 2024 and 1993 cm^{-1} obtained at 450 °C are of particular interest. We applied AIMD slab calculations (see Supporting Information and Figure 4b) to elucidate the nature of these absorptions. Both RhCO and $Rh(CO)_2$ remain stable at the surface during the complete simulation (up to 45 ps). Additionally, vibrational power spectra (Figure 4b) were calculated. We found that the calculated spectra are in excellent agreement with the experimental spectrum for the Ga_{88}−Rh_1 sample above 300 °C. They show a feature at 1993 cm^{-1} for RhCO and two bands at 2002 and 1978 cm^{-1} for the symmetric and asymmetric CO-stretching frequencies of $Rh(CO)_2$, respectively. Based on this data, we identify two possible explanations for the experimental observations. On the one hand, the signal at 2024 cm^{-1} may be assigned to hydrides bound on metallic Ga (Ga−H peak found at 2021 cm^{-1} in the case of the monometallic Ga/Al_2O_3 sample, compare also Table 1), while the peak at 1993 cm^{-1} originates from a CO stretching vibration of a RhCO species. On the other hand, the DFT results also are in agreement with the formation of a $Rh(CO)_2$ species. In the latter case, the two experimental peaks would be ascribed to the symmetric and asymmetric CO-stretching modes. From the experimental and theoretical data, both interpretations appear reasonable, as the peak positions of $Rh^I(CO)_2$ (symmetric CO stretch) and Ga−H bands both lie around 2025 cm^{-1} and the features may overlap.

The effect of site isolation on the CO-stretching frequency is evaluated by performing frequency calculations in harmonic approximation for CO at a Rh top-site on a perfect Rh(111) surface at different coverages. The results as shown in Table 1 are in line with previously calculated values,[32,33] which show that the frequency is strongly coverage dependent. Compared to the experimental data, the DFT values are in excellent agreement at a high coverage, while being ~20 cm^{-1} too low at lower coverage.[34] Therefore, we conclude that the main contribution to the redshift in the vibrational spectra of the Rh−Ga mixtures originates from the isolation of the Rh atoms.

The spectra obtained from the Ga_{88}−Rh_1 and Ga_{125}−Rh_1 (see Supporting Information, Figure S26) samples recorded at 400 and 450 °C show only two peaks, which are assigned to Ga−H species and/or $Rh(CO)_{1-2}$ in liquid Ga. There is no evidence for adsorbed CO on Rh atoms interacting with the support or for the formation of larger Rh clusters. Thus, the thermal evolution of the DRIFT spectra provides further evidence for the presence of a liquid Ga phase with isolated Rh atoms exposed at the surface. Figure 6 illustrates our conclusions from infrared spectroscopy and DFT calculation for the different Ga−Rh samples under investigation.

Discussion. Merging the information given for the phase behavior of the Ga−Rh system,[11] the solubility data of Rh in Ga,[35] the analytical data and additional catalytic experiments described here (see Supporting Information for details), it is possible to correlate the physical states of the different materials at varying Ga/Rh ratios with their catalytic properties. In Figure 7, the productivity values obtained when applying different compositions of SCALMS at different temperatures are depicted versus the known phase diagram

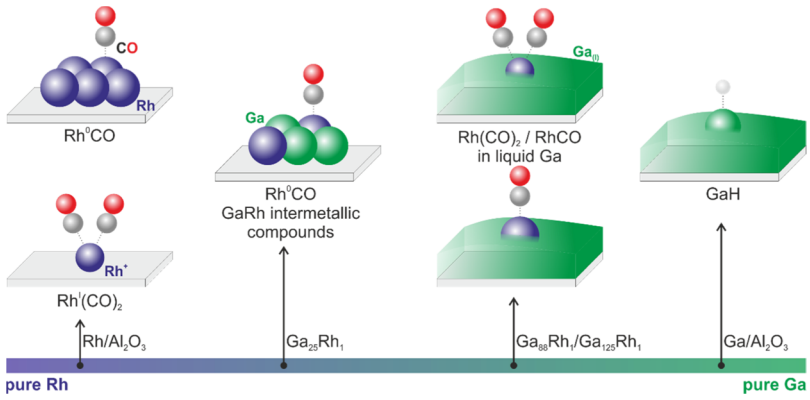

Figure 6. Surface features observed on the Ga_x−Rh_y SCALMS and on the Rh/Al_2O_3 and Ga/Al_2O_3 reference samples.

DOI: 10.1021/acscatal.9b02459
ACS Catal. 2019, 9, 9499−9507

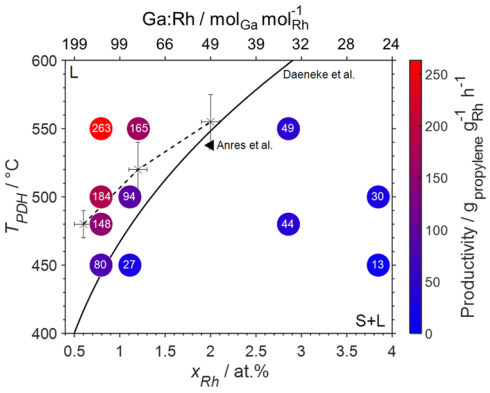

Figure 7. Productivities after 12 min time on stream (numbers in circles) from the various Ga−Rh SCALMS compositions at different temperatures superimposed on the liquidus line of the Ga−Rh phase diagram (solid) according to Daeneke et al.,[35] an experimental data point for the solubility of Rh in Ga (filled triangle) by Anres et al.,[11] as well as the experimentally obtained solubility data from herein conducted XPS measurements (crosses connected by the dashed line to guide the eye).

data and the data from our XPS experiments. According to our XPS and TEM data, systems with a Ga−Rh ≤ 33 are characterized by the presence of solid intermetallic Rh−Ga phases, together with a Ga-rich liquid phase (vide infra) and can be expected to never reach a fully liquid state, at any of the temperatures tested. Conversely, the system with Ga−Rh > 120 is expected to be always present in the fully liquid phase under the applied reaction conditions forming a liquid alloy. The systems with 82 < Ga−Rh ≤ 89 may be defined as borderline cases as the liquidus line is crossed at a temperature between 450 and 500 °C. Hence, these systems are expected to be fully liquid at 550 °C. Figure 7 shows that the productivities are always significantly higher in the case of fully liquid Ga−Rh SCALMS systems, irrespective of the applied reaction temperature (compare results at 480, 500, and 550 °C). In other words, the catalyst with $Ga_{125}Rh$ showed the highest performance for the whole set of temperatures, as its fully liquid nature allows for the maximum presence of single Rh atoms at the liquid/gas interface (vide infra). The catalysts with Ga−Rh ≤ 33.5, conversely, showed for all temperatures the poorest performance, as a significant part of the Rh is always present in solid intermetallic phases, showing lower catalytic activity in these systems.

CONCLUSIONS

While hardly any successful example of Rh-catalyzed alkane dehydrogenation catalysis is known, we show in this paper that supported Ga−Rh alloys are a very interesting class of PDH catalysts. Even small additions of Ga to alumina-supported Rh have a positive effect on the catalytic activity and selectivity. A strong boost of the Rh-induced dehydrogenation activity was found under conditions where the supported Ga−Rh alloy is entirely liquid.

Moreover, our paper sheds light on the chemical nature and working principles of Rh-based dehydrogenation catalysis in supported Ga−Rh alloys. From our AIMD simulations, we conclude that the liquid metal interface is highly dynamic whereby Rh appears at the interface only periodically and is trapped there for a longer time if propane is offered from the gas phase. Additionally, our calculations suggest a cooperative mode of action between Ga and Rh during catalysis with the activation of the propane at the Rh single-site atom, followed by transfer of the propyl rest to the Ga surface while recombination of two hydrides to H_2 occurs at the Rh single site. Our infrared studies confirm the single atom nature of Rh at the liquid interface.

All our results provide additional evidence that the specific nature of supported liquid Ga alloys offers very beneficial properties for dehydrogenation catalysis. This remarkable fact encourages us to extend this particular material strategy to explore other Ga alloy systems and substrates in our ongoing work.

ASSOCIATED CONTENT

Supporting Information

The Supporting Information is available free of charge on the ACS Publications website at DOI: 10.1021/acscatal.9b02459.

Materials synthesis, reactor, and analytic description, SEM, XPS, and Raman characterization of catalysts, TEM, DFT methods, and DRIFT set-up description (PDF)

Video S1. Electron diffraction series of sample with x = 36, temperature 400−530 °C, 20× accelerated (AVI)

Video S2. Electron diffraction series of sample with x = 105, temperature 550−RT °C, 20× accelerated (AVI)

AUTHOR INFORMATION

Corresponding Author

*E-mail: peter.wasserscheid@fau.de.

ORCID

Moritz Wolf: 0000-0002-1326-5337
Tanja Bauer: 0000-0002-6399-2954
Marco Haumann: 0000-0002-3896-365X
Christian Papp: 0000-0002-1733-4387
Andreas Görling: 0000-0002-1831-3318
Jörg Libuda: 0000-0003-4713-5941
Hans-Peter Steinrück: 0000-0003-1347-8962
Peter Wasserscheid: 0000-0003-0413-9539

Author Contributions

¶N.R. and S.M. shared first authorship.

Notes

The authors declare no competing financial interest.

ACKNOWLEDGMENTS

The authors gratefully acknowledge the funding of the German Research Council (DFG), which, within the framework of its "Excellence Initiative" supports the Cluster of Excellence "Engineering of Advanced Materials" (www.eam.fau.de) at the Friedrich-Alexander-Universität Erlangen-Nürnberg (FAU). Furthermore, N.R., N.T., M. Wolf, M.H., and P.W. acknowledge support by the European Research Foundation through the ERC AIG "SCALMS" (grant no. 786475).

REFERENCES

(1) Taccardi, N.; Grabau, M.; Debuschewitz, J.; Distaso, M.; Brandl, M.; Hock, R.; Maier, F.; Papp, C.; Erhard, J.; Neiss, C.; Peukert, W.; Görling, A.; Steinrück, H. P.; Wasserscheid, P. Gallium-rich Pd-Ga phases as supported liquid metal catalysts. *Nat. Chem.* **2017**, *9*, 862−867.

DOI: 10.1021/acscatal.9b02459
ACS Catal. 2019, 9, 9499−9507

(2) Kettner, M.; Maisel, S.; Stumm, C.; Schwarz, M.; Schuschke, C.; Görling, A.; Libuda, J. Pd-Ga model SCALMS: Characterization and stability of Pd single atom sites. *J. Catal.* **2019**, *369*, 33−46.
(3) Bauer, T.; Maisel, S.; Blaumeiser, D.; Vecchietti, J.; Taccardi, N.; Wasserscheid, P.; Bonivardi, A.; Görling, A.; Libuda, J. Operando DRIFTS and DFT Study of Propane Dehydrogenation over Solid- and Liquid-Supported GaxPty Catalysts. *ACS Catal.* **2019**, *9*, 2842−2853.
(4) Upham, D. C.; Agarwal, V.; Khechfe, A.; Snodgrass, Z. R.; Gordon, M. J.; Metiu, H.; McFarland, E. W. Catalytic molten metals for the direct conversion of methane to hydrogen and separable carbon. *Science* **2017**, *358*, 917−921.
(5) Ogino, Y. *Catalysis and Surface Properties of Liquid Metals and Alloys*; Marcel Dekker: New York, 1987.
(6) Zhang, J.; Hosemann, P.; Maloy, S. Models of liquid metal corrosion. *J. Nucl. Mater.* **2010**, *404*, 82−96.
(7) Sattler, J. J. H. B.; Ruiz-Martinez, J.; Santillan-Jimenez, E.; Weckhuysen, B. M. Catalytic Dehydrogenation of Light Alkanes on Metals and Metal Oxides. *Chem. Rev.* **2014**, *114*, 10613−10653.
(8) Resasco, D. E.; Haller, G. L. Novel rhodium/titania and iridium/titania catalysts for n-butane isomerization and dehydrogenation. *J. Phys. Chem.* **1984**, *88*, 4552−4556.
(9) Solymosi, F.; Tomalcsov, P.; Kedves, K. CO2 reforming of propane over supported Rh. *J. Catal.* **2003**, *216*, 377−385.
(10) Ferretti, O. A.; Siri, G. J.; Humblot, F.; Candy, J. P.; Didillon, B.; Basset, J. M. Improvements In Selectivity And Stability Of Rh Catalysts Modified By SnBu4 Dehydrogenation Of Isobutane To Isobutene. *React. Kinet. Catal. Lett.* **1998**, *63*, 115−120.
(11) Anres, P.; Gaune-Escard, M.; Bros, J. P. Thermodynamics of the (Rh−Ga) system. *J. Alloys Compd.* **1998**, *265*, 201−208.
(12) Schreiber, M. W.; Plaisance, C. P.; Baumgärtl, M.; Reuter, K.; Jentys, A.; Bermejo-Deval, R.; Lercher, J. A. Lewis−Brønsted Acid Pairs in Ga/H-ZSM-5 To Catalyze Dehydrogenation of Light Alkanes. *J. Am. Chem. Soc.* **2018**, *140*, 4849−4859.
(13) Searles, K.; Chan, K. W.; Burak, J. A. M.; Zemlyanov, D.; Safonova, O.; Copéret, C. Highly Productive Propane Dehydrogenation Catalyst Using Silica-Supported Ga−Pt Nanoparticles Generated from Single-Sites. *J. Am. Chem. Soc.* **2018**, *140*, 11674−11679.
(14) Redekop, E. A.; Galvita, V. V.; Poelman, H.; Bliznuk, V.; Detavernier, C.; Marin, G. B. Delivering a Modifying Element to Metal Nanoparticles via Support: Pt−Ga Alloying during the Reduction of Pt/Mg(Al,Ga)Ox Catalysts and Its Effects on Propane Dehydrogenation. *ACS Catal.* **2014**, *4*, 1812−1824.
(15) Föttinger, K. The effect of CO on intermetallic PdZn/ZnO and Pd_2Ga/Ga_2O_3 methanol steam reforming catalysts: A comparative study. *Catal. Today* **2013**, *208*, 106−112.
(16) Grabau, M.; Erhard, J.; Taccardi, N.; Calderon, S. K.; Wasserscheid, P.; Görling, A.; Steinrück, H.-P.; Papp, C. Spectroscopic Observation and Molecular Dynamics Simulation of Ga Surface Segregation in Liquid Pd-Ga Alloys. *Chem.—Eur. J.* **2017**, *23*, 17701−17706.
(17) Okamoto, H. Ga-Rh (Gallium-Rhodium). *J. Phase Equilib.* **1999**, *20*, 538.
(18) Qi, W. Nanoscopic Thermodynamics. *Acc. Chem. Res.* **2016**, *49*, 1587−1595.
(19) Henkelman, G.; Uberuaga, B. P.; Jónsson, H. A climbing image nudged elastic band method for finding saddle points and minimum energy paths. *J. Chem. Phys.* **2000**, *113*, 9901−9904.
(20) Henkelman, G.; Jónsson, H. A dimer method for finding saddle points on high dimensional potential surfaces using only first derivatives. *J. Chem. Phys.* **1999**, *111*, 7010.
(21) Bechthold, P.; Ardhengi, J. S.; Juan, A.; González, E. A.; Jasen, P. V. CO adsorption on PdGa(1 0 0), (1 1 1) and$(\bar{1}\ \bar{1}\ \bar{1})$ surfaces: A DFT study. *Surf. Sci.* **2014**, *315*, 467−474.
(22) Prinz, J.; Gaspari, R.; Stöckl, Q. S.; Gille, P.; Armbrüster, M.; Brune, H.; Gröning, O.; Pignedoli, C. A.; Passerone, D.; Widmer, R. Ensemble Effect Evidenced by CO Adsorption on the 3-Fold PdGa Surfaces. *J. Phys. Chem. C* **2014**, *118*, 12260−12265.
(23) Bechthold, P.; Jasen, P. V.; Ardenghi, J. S.; González, E. A.; Juan, A. Ab initio study of CO adsorption on PdGa(110). *Comput. Mater. Sci.* **2013**, *71*, 192−196.
(24) Armbrüster, M.; Schlögl, R.; Grin, Y. Intermetallic compounds in heterogeneous catalysis-a quickly developing field. *Sci. Technol. Adv. Mater.* **2014**, *15*, 034803.
(25) Collins, S.; Baltanás, M. A.; Garcia Fierro, J. L.; Bonivardi, A. L. Gallium-Hydrogen Bond Formation on Gallium and Gallium-Palladium Silica-Supported Catalysts. *J. Catal.* **2002**, *211*, 252−264.
(26) Bulushev, D. A.; Froment, G. F. A DRIFTS study of the stability and reactivity of adsorbed CO species on a Rh/γ-Al_2O_3 catalyst with a very low metal content. *J. Mol. Catal. A: Chem.* **1999**, *139*, 63−72.
(27) Zaki, M. I.; Tesche, B.; Kraus, L.; Knözinger, H. Supported rhodium catalysts. Support effects on state and dispersion of the rhodium. *Surf. Interface Anal.* **1988**, *12*, 239−246.
(28) Finocchio, E.; Busca, G.; Forzatti, P.; Groppi, G.; Beretta, A. State of Supported Rhodium Nanoparticles for Methane Catalytic Partial Oxidation (CPO): FT-IR Studies. *Langmuir* **2007**, *23*, 10419−10428.
(29) Solymosi, F.; Knözinger, H. Infrared study on the interaction of CO with alumina-supported rhodium. *J. Chem. Soc., Faraday Trans.* **1990**, *86*, 389−395.
(30) Trautmann, S.; Baerns, M. Infrared Spectroscopic Studies of CO Adsorption on Rhodium Supported by SiO_2, Al_2O_3, and TiO_2. *J. Catal.* **1994**, *150*, 335−344.
(31) Hadjiivanov, K.; Ivanova, E.; Dimitrov, L.; Knözinger, H. FTIR spectroscopic study of CO adsorption on Rh−ZSM-5: detection of Rh^+−CO species. *J. Mol. Struct.* **2003**, *661−662*, 459−463.
(32) Köhler, L.; Kresse, G. Density functional study of CO on Rh(111). *Phys. Rev. B: Condens. Matter Mater. Phys.* **2004**, *70*, 165405.
(33) Krenn, G.; Bako, I.; Schennach, R. CO adsorption and CO and O coadsorption on Rh(111) studied by reflection absorption infrared spectroscopy and density functional theory. *J. Chem. Phys.* **2006**, *124*, 144703.
(34) Linke, R.; Curulla, D.; Hopstaken, M. J. P.; Niemantsverdriet, J. W. CO/Rh(111): Vibrational frequency shifts and lateral interactions in adsorbate layers. *J. Chem. Phys.* **2001**, *115*, 8209.
(35) Daeneke, T.; Khoshmanesh, K.; Mahmood, N.; de Castro, I. A.; Esrafilzadeh, D.; Barrow, S. J.; Dickey, M. D.; Kalantar-zadeh, K. Liquid metals: fundamentals and applications in chemistry. *Chem. Soc. Rev.* **2018**, *47*, 4073−4111.

DOI: 10.1021/acscatal.9b02459
ACS Catal. 2019, 9, 9499−9507